

Fragment-based strategy for structural optimization in combination with 3D-QSAR

Haoliang Yuan · Wenting Tai · Shihe Hu · Haichun Liu ·
Yanmin Zhang · Sihui Yao · Ting Ran · Shuai Lu · Zhipeng Ke ·
Xiao Xiong · Jinxing Xu · Yadong Chen · Tao Lu

Received: 2 August 2013 / Accepted: 24 October 2013 / Published online: 1 November 2013
© Springer Science+Business Media Dordrecht 2013

Abstract Fragment-based drug design has emerged as an important methodology for lead discovery and drug design. Different with other studies focused on fragment library design and active fragment identification, a fragment-based strategy was developed in combination with three-dimensional quantitative structure–activity relationship (3D-QSAR) for structural optimization in this study. Based on a validated scaffold or fragment hit, a series of structural optimization was conducted to convert it to lead compounds, including 3D-QSAR modelling, active site analysis, fragment-based structural optimization and evaluation of new molecules. 3D-QSAR models and active site analysis provided sufficient information for confirming the SAR and pharmacophoric features for fragments. This strategy was evaluated through the structural optimization

on a c-Met inhibitor scaffold 5H-benzo[4,5]cyclohepta[1,2-b]pyridin-5-one, which resulted in an c-Met inhibitor with high inhibitory activity. Our study suggested the effectiveness of this fragment-based strategy and the druggability of our newly explored active region. The reliability of this strategy indicated it could also be applied to facilitate lead optimization of other targets.

Keywords Fragment-based drug design · 3D-QSAR · c-Met · Lead discovery · Structural optimization

Introduction

Fragment-based drug design (FBDD) has been considered as a promising methodology for lead discovery and structural optimization. In parallel to the increasing interest in experimental FBDD, computational FBDD has also attracted many spotlights due to its effectiveness and efficiency [1, 2]. Many computational FBDD strategies have been developed by targeting main bottlenecks of FBDD, including library design, fragment hit identification and subsequent optimization into leads [3–5].

Most of the current FBDD strategies usually focused on fragment library design and fragment hit identification [2, 6, 7]. Small molecules with molecular mass of 350 Da or less, defined as scaffolds, give chemists better starting points of avoiding problems with favorable physicochemical properties during lead optimization. Once the good fragment starting points and exact information on how the fragment binds to the active site are obtained, structural optimization is needed to drive the fragment hits into leads. This process poses great challenges, even for the most promising starting point [3]. Consequently, a rational and

Haoliang Yuan and Wenting Tai have contributed equally to this work.

Electronic supplementary material The online version of this article (doi:10.1007/s10822-013-9687-x) contains supplementary material, which is available to authorized users.

H. Yuan · W. Tai · S. Hu · H. Liu · Y. Zhang · S. Yao ·
T. Ran · S. Lu · Z. Ke · X. Xiong · J. Xu · Y. Chen (✉) ·
T. Lu (✉)

Laboratory of Molecular Design and Drug Discovery,
School of Science, China Pharmaceutical University,
24 Tongji Xiang, Nanjing 210009, China
e-mail: ydchen@cpu.edu.cn

T. Lu
e-mail: lutao@cpu.edu.cn

T. Lu
State Key Laboratory of Natural Medicines, China
Pharmaceutical University, 24 Tongji Xiang,
Nanjing 210009, China

reliable strategy is essential to shorten the process of structural optimization. Aside from fragment library design and fragment hit identification, fragment-based strategies for structural optimization should also be highlighted for the process of scaffolds to leads.

During fragment optimization, information on how the fragment binds to the active site is very important [8]. Even when binding mode of the scaffold is experimentally confirmed, the requirements of physicochemical and pharmacophoric properties for substituted fragments on the scaffold are critical in the process of scaffolds to leads. Therefore, active site analysis is necessary for scaffold optimization. When a series of compounds derived from a common scaffold were obtained, three-dimensional quantitative structure–activity relationship (3D-QSAR) analysis is a commonly used approach to provide the structure–activity relationship (SAR) [9, 10]. In this study, a structural optimization strategy is proposed using fragment-based approaches in combination with 3D-QSAR.

This strategy was evaluated through a case study on c-Met inhibitors with a scaffold of 5H-benzo[4,5]cyclohepta[1,2-b]pyridin-5-one [11]. C-Met (i.e. mesenchymal-epithelial transition factor), a receptor tyrosine kinase, with its natural ligand, hepatocyte growth factor (HGF), is involved in cell proliferation, migration, and invasion, which are essential for normal embryonic development. However, c-Met is deregulated and associated with high tumor grade and poor prognosis in a number of human cancers. Several mechanisms lead to deregulation, including the overexpression of c-Met and/or HGF, amplification of the Met gene, or activating mutations of c-Met, all of which have been found in human cancers. Although some potent inhibitors have been developed based on different scaffolds targeting c-Met [12], there have been several

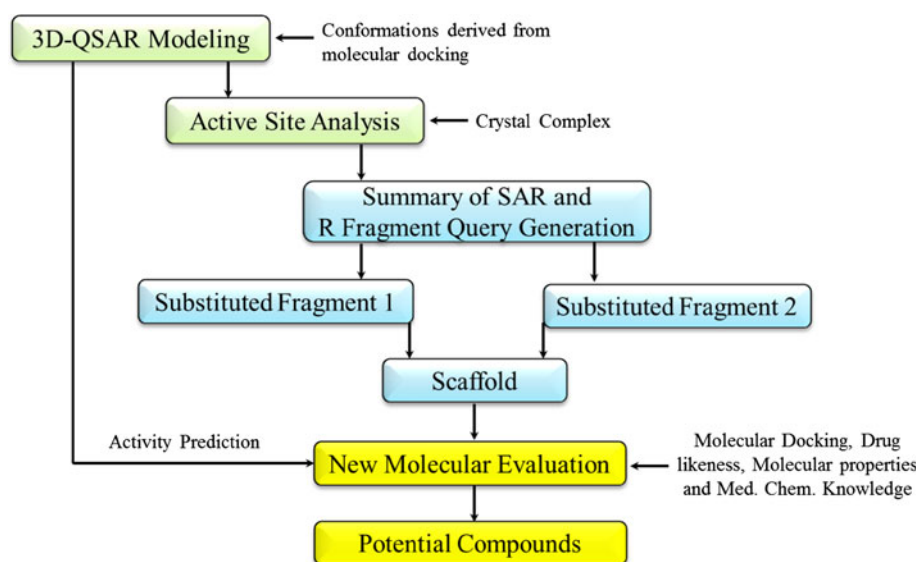
reports in the literature of oncogenic mutations of c-Met that confer resistance to small molecule inhibitors of c-Met [13–17]. A series of compounds derived from the scaffold of 5H-benzo[4,5]cyclohepta[1,2-b]pyridin-5-one were reported to maintain potency against a spectrum of the mutations [11]. Although there have been no reports discussing these mutations with respect to treatment in a clinical setting, it stands a reason that a compound that was insensitive to acquired mutations in the kinase might have certain advantage in the treatment of c-Met dependent tumors [16, 18]. Thus, compounds derived from the scaffold of 5H-benzo[4,5]cyclohepta[1,2-b]pyridin-5-one are promising for overcoming the resistance. It is worthwhile for further structural optimization on this scaffold. In this study, this scaffold was selected as the starting point for structural optimization with the purpose to validate the fragment-based strategy and pursue for better potent c-Met inhibitors.

Materials and methods

Overview of the current strategy

An overview of the fragment-based strategy for structural optimization is schematically described in Fig. 1. A series of compounds with 5H-benzo[4,5]cyclohepta[1,2-b]pyridin-5-one were superimposed using their docking conformations. Active site analysis was performed based on the crystal complex structure using different programs. Based on 3D-QSAR studies and active site analysis, critical pharmacophoric features were confirmed for different substituted fragments. They were used as search queries in the process of substituted fragment identification,

Fig. 1 Workflow for the fragment-based structural optimization strategy in combination with 3D-QSAR



respectively. Different fragments obtained were added to the scaffold on the corresponding substituted points. 3D-QSAR activity prediction and other criteria like Lipinski's "Rule of 5" [19] were used for potential compounds selection. The details of each step are described in the subsequent sections.

Dataset preparation

A set of 55 c-Met inhibitors derived from the scaffold [11] was obtained from published data, which covered reasonable chemical diversity and biological activity. For developing 3D-QSAR models, the training and test set compounds should both span at least four orders of activity magnitude. They should be also well-proportioned in each activity magnitude. With these basic rules, these compounds were randomly divided into the training set and test set (Table 1). The training set consisted of 44 compounds spanning four orders of activity magnitude was used to generate the QSAR models. The left 11 compounds constituted the test set. Their IC_{50} values were converted to pIC_{50} ($-\log IC_{50}$), which would be used as dependent variables for subsequent 3D-QSAR analysis.

Molecular modeling and alignment

3D structures of the compounds were constructed within the sketch module and atom types of each molecule were carefully checked in Sybyl6.9. *Gasteiger-Hückel* charges were added to them before promoted to energy minimization using the Tripos standard force field. Molecular alignment is the most sensitive factor which has a significant impact on the 3D-QSAR models. In this study, by simulating the binding conformations of the compounds, molecular alignment was obtained through molecular docking. Thus, all the molecules were aligned well in the binding site for developing 3D-QSAR models.

Molecular docking

There were two co-crystal complex structures of 5H-benzo[4,5]cyclohepta[1,2-b]pyridin-5-one inhibitors available in Protein Data Bank (PDB), 3R7O and 3Q6W [20]. These two complex structures were both used for docking. Considering the alignment of docking conformations, the better one would be selected as the receptor structure for subsequent molecular docking using Glide 5.0 implemented in Schrödinger. Glide has shown good reproducibility of co-crystal ligand conformations, which has also been recommended in some literature reports for its accuracy in molecular docking and scoring [21, 22]. The complex structure obtained from PDB was firstly prepared with the Protein Preparation Wizard workflow. All the

water molecules were removed. The binding region was defined by a 12 Å_12 Å_12 Å box centred in the centroid of the crystal ligand. All other parameters were kept as default. The best pose was output on the basis of Glide score and the protein–ligand interactions. The extra precision (XP) mode was used for the docking and scoring.

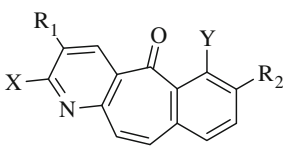
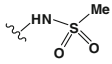
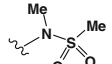
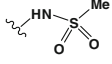
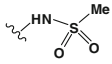
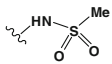
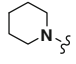
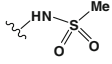
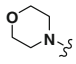
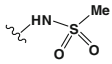
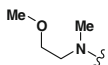
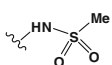
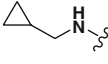
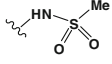
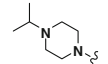
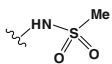
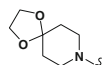
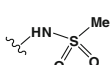
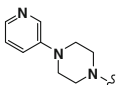
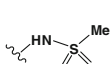
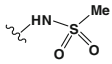
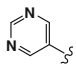
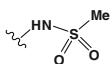
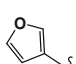
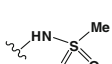
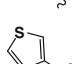
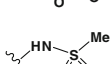
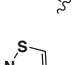
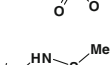
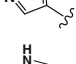
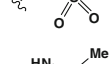
3D-QSAR model construction

The classical 3D-QSAR modelling approaches, including Comparative Molecular Field Analysis (CoMFA) and Comparative Molecular Similarity Indices Analysis (CoMSIA), were applied for structure–activity relationship study. Both CoMFA and CoMSIA models were carried out using the QSAR module in Sybyl6.9. The standard Tripos force fields in Sybyl6.9 were employed for CoMFA and CoMSIA analysis. To derive CoMFA descriptors fields, a hybridized sp^3 carbon atom with a charge of +1.0 and van der Waals radius of 1.53 Å was employed as a probe to compute the steric (S) and electrostatic (E) energies between the probe and the compounds. For CoMSIA analysis, by using a sp^3 carbon atom probe with a charge of +1.0, five similarity indices consisting of steric (S), electrostatic (E), hydrophobic (H), hydrogen bond donor (D), and hydrogen bond acceptor (A) fields were calculated for each lattice with a grid of 2 Å. The optimal number of components was designated such that cross-validated r_{cv}^2 was maximal and the standard error of prediction was minimal. CoMSIA, using Gaussian-type distance dependence, provides smooth and interpretable contour maps. A default value of 0.3 was used as the attenuation factor.

Partial least square (PLS) analysis

Partial least squares (PLS) analysis was used to linearly correlate the CoMFA and CoMSIA fields to the binding affinity values. The descriptors of CoMFA and CoMSIA were used as independent variables, and pIC_{50} activity values were used as dependent variables. The cross-validation analysis was performed using leave-one-out (LOO) method, in which one compound is removed from the dataset, and its activity can be then predicted using the model derived from the rest compounds of the dataset. The model that resulted in the highest cross validated r_{cv}^2 , optimum number of components and the lowest standard error of prediction were taken for further analysis. To speed up the analysis and reduce noise, a minimum column filter value σ (2.00 kcal/mol) was used. A final analysis was performed to calculate conventional r_{ncv}^2 using the optimum number of components obtained from the cross-validation analysis. In addition, the statistical significance of the models was described by the standard error of estimate (SEE) and probability value (F value).

Table 1 Structures and experimental inhibitory activities of the data set for 3D-QSAR modeling

						
Compd.	R ₁	X	R ₂	Y	IC ₅₀ (nM)	pIC ₅₀
1	Phenyl	H		H	31	7.51
2	Phenyl	H	H	NH ₂	1,100	5.96
3	Phenyl	H		H	780	6.11
4	Cl	H		H	380	6.42
5	H	H		H	1,100	5.96
6	Phenyl	NH ₂		H	6,100	5.21
7 ^a		H		H	93	7.03
8		H		H	46	7.33
9		H		H	440	6.36
10		H		H	89	7.05
11		H		H	32	7.49
12 ^a		H		H	24	7.62
13		H		H	16	7.80
14 ^a	4-Chlorophenyl	H		H	46	6.55
15		H		H	180	6.74
16		H		H	64	7.19
17		H		H	10	8.00
18		H		H	14	7.85
19 ^a		H		H	170	6.77

^a Test set compounds

Table 1 continued

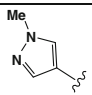
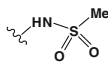
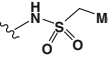
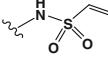
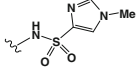
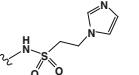
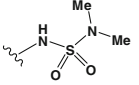
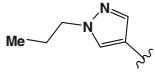
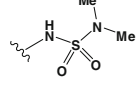
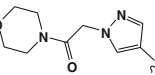
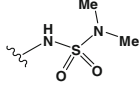
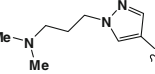
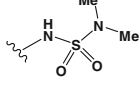
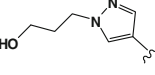
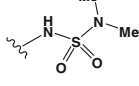
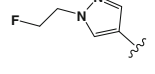
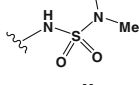
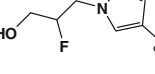
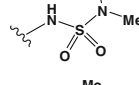
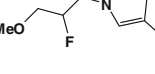
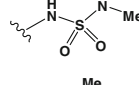
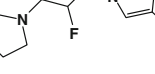
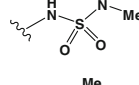
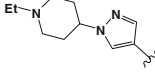
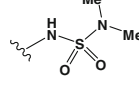
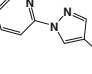
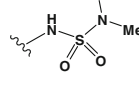
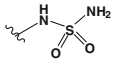
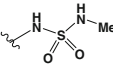
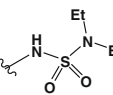
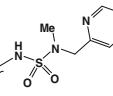
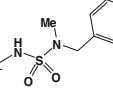
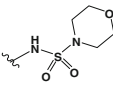
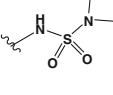
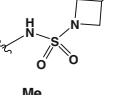
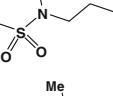
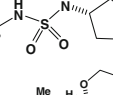
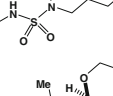
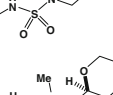
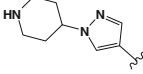
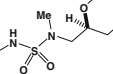
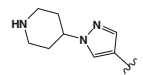
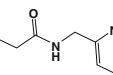
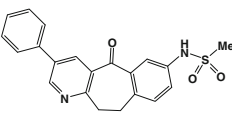
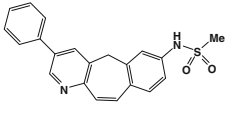
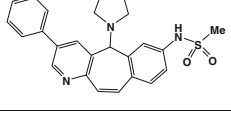
20		H		H	4	8.40
21	<i>N</i> -methylpyrazole	H	–NH ₂	Cl	19	7.72
22	<i>N</i> -methylpyrazole	H	–NHMe	H	5	8.30
23 ^a	<i>N</i> -methylpyrazole	H	–OH	H	11	7.96
24	Phenyl	H		H	27	7.57
25	Phenyl	H		H	130	6.89
26	<i>N</i> -methylpyrazole	H		H	100	7.00
27	<i>N</i> -methylpyrazole	H		H	13	7.89
28 ^a	<i>N</i> -methylpyrazole	H		H	4	8.40
29		H		H	2	8.70
30		H		H	2	8.70
31		H		H	4	8.40
32		H		H	3	8.52
33		H		H	3	8.52
34 ^a		H		H	1	9.00
35		H		H	3	8.52
36		H		H	2	8.70
37		H		H	0.2	9.70
38		H		H	130	6.89

Table 1 continued

39	<i>N</i> -methylpyrazole	H		H	3	8.52
40 ^a	<i>N</i> -methylpyrazole	H		H	2	8.70
41	<i>N</i> -methylpyrazole	H		H	4	8.40
42	<i>N</i> -methylpyrazole	H		H	2	8.70
43 ^a	<i>N</i> -methylpyrazole	H		H	30	7.52
44	<i>N</i> -methylpyrazole	H		H	58	7.24
45	<i>N</i> -methylpyrazole	H		H	10	8.00
46	<i>N</i> -methylpyrazole	H		H	5	8.30
47	<i>N</i> -methylpyrazole	H		H	3	8.52
48 ^a	<i>N</i> -methylpyrazole	H		H	2	8.70
49	<i>N</i> -methylpyrazole	H		H	14	7.85
50	<i>N</i> -methylpyrazole	H		H	2	8.70
51		H		H	2.6	8.59
52		H		H	28	7.55
53 ^a					2,300	5.64
54					2,800	5.55
55					770	6.11

^a Test set compounds

3D-QSAR model validation

The predictive capability of the 3D-QSAR models was evaluated with an external test set of eleven molecules. The test set molecules were also optimized and aligned in the same manner as described above, and their activities were predicted using the developed models. The predictive correlation (r_{pred}^2) based on the test set molecules, is computed using Eq. (1):

$$\begin{aligned}\text{PRESS} &= \sum (Y_{\text{actual}} - Y_{\text{predicted}})^2 \\ \text{SD} &= \sum (Y_{\text{actual}} - Y_{\text{mean}})^2 \\ r_{\text{pred}}^2 &= (\text{SD} - \text{PRESS}) / \text{SD}\end{aligned}\quad (1)$$

where $Y_{\text{predicted}}$, Y_{actual} , Y_{mean} are the predicted, actual and mean values of pIC_{50} . SD is the sum of the squared deviations between the biological activities of the test set and mean activities of the training set molecules and PRESS is the sum of squared deviation between predicted and actual activity values for every molecule in the test set.

Active site analysis

An analysis on the active site will provide information on protein–ligand interaction and the specific pharmacophoric features required by the adjacent amino acid residues. The *Ligand Interactions* module implemented in MOE 2009 is such a tool can be applied for active site analysis. It provides a means to visualize an active site of a complex in a diagrammatic form. The panel will assist structure optimization by providing insights into protein–ligand interactions and enhance receptor complementarity. Another program for active site analysis is the *Sitemap* module implemented in Schrodinger 2009 [23]. *Sitemap* generates information on the characteristics of binding site using novel search and analysis facilities. It will give site points to occupy the active site, and display hydrophobic and hydrophilic site maps, including hydrogen bond donor, acceptor and metal-binding regions. Accordingly, *Sitemap* can provide useful information on the active site features and aid the design of better ligands.

Fragment-based structural optimization

A clean Zinc fragment library containing 390,600 fragments was used for fragment identification. This fragment library was “washed” and energy minimized in MOE 2009. After 3D-QSAR modeling and active site analysis, the physico-chemical properties and pharmacophoric features for the different substituted fragments were confirmed. With the information, pharmacophore query and property filters were applied in the process of fragment identification. The

integrated *scaffold replacement* module was used to add these fragments onto corresponding substituted points respectively. *BREED* module was used in series to create new molecules by the substituted fragments hybrid [24]. The input molecules share the same scaffold, thus the new structures should preserve intra molecular orientations as closely as possible. In the process of *BREED*, a collection of 2D and 3D properties were calculated to evaluate the lead- or drug-likeness. The receptor is also present to refine the new structures in the binding site.

Evaluation of new structures

New molecules were firstly docked into the active site with XP mode. Molecules with reasonable binding mode were kept for activity prediction. The scaffold should be almost in the original spatial place and other substituted fragments should also satisfy the requirements in the active site. Molecules passed the docking filter will be predicted with the developed 3D-QSAR models. Since the output activity is pIC_{50} , new molecules with an activity value bigger than 9.0 were further analyzed by comparing with known inhibitors for potential ones.

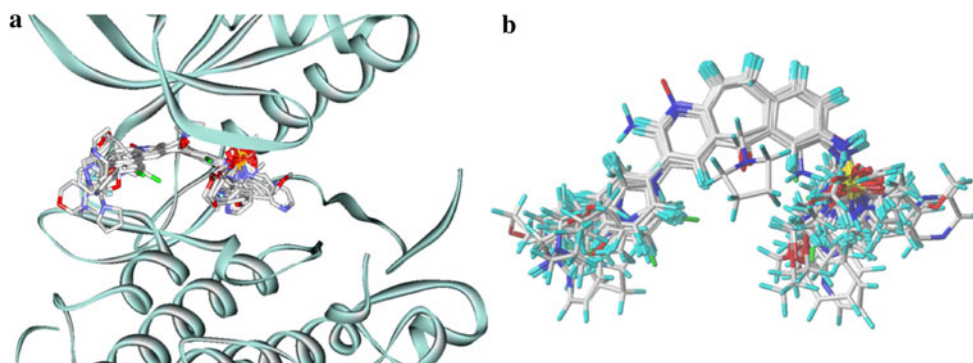
Results and discussion

Fragment-based strategy for structural optimization in combination with 3D-QSAR

Fragment-based methods have been applied in structural optimization in many studies [25–30]. The successful conversions from fragment hits to lead compounds and even clinical candidates have attracted many researchers to investigate fragment-based drug design and the applications [31, 32]. Many fragment-based approaches have been reported [2, 33, 34]. Generally, a fragment library of high quality is firstly designed and then biophysical or computational approaches are applied to screen to find fragment hits. The fragment hits can be substructure query to search commercial library to obtain bigger compounds for bioassays [35]. Alternatively, experimental approaches can be applied to sequentially detect the binding modes of the fragment derivatives for lead compounds [36]. Most of current fragment-based strategies focus on fragment library design and fragment hit identification, while structural optimization has not been widely studied. This phase should be also emphasized by fragment-based strategies.

Herein, a novel fragment-based strategy was developed for structural optimization in combination with 3D-QSAR in this study. Given a validated scaffold or fragment hit, structural optimization will be used to convert it to lead compounds. In some studies, single substituted groups could be replaced by using suitable approaches [37], however, if

Fig. 2 Molecular alignment based on the docking conformations



two or multiple groups on the scaffold could be replaced simultaneously by suitable fragments, it will generate more diversified compounds and larger chemical space. This hypothesis was carried out in this study by using *add R group to ligand* and *BREED* modules in series. The first premise for this strategy is to identify suitable fragments on different substituted points. 3D-QSAR modeling and active site analysis were applied to get SAR and validated 3D-QSAR models were used for activity prediction. Besides, requirements about physicochemical properties and pharmacophoric features of different regions in the active site would also be obtained to find suitable fragments on the corresponding substituted positions. Evaluation of new molecules with molecular docking and activity prediction may have great potential identify the potential compounds.

3D-QSAR modeling

Molecular alignment

The quality and predictive ability of the models are directly dependent on the molecular alignment. The 3D-QSAR models are constructed based on the assumption that 3D structures of input compounds are aligned using their biologically active conformations. It has been widely applied to simply align the molecules based on their common substructure. However, this may not reflect the bioactive conformations of the inhibitor as different conformations may be adopted due to various substituted groups. Thus, the conformations used to construct 3D-QSAR models should be as similar as possible with their bioactive conformations. Molecular docking is considered as an effective approach for simulating the binding conformation of the inhibitors in the target binding site. Hence, the inhibitors used for developing 3D-QSAR models were aligned using their docking conformations. Besides, the docking conformations would facilitate understanding the different fields of the models. Docking conformations of the molecules aligned better using 3R7O. From Fig. 2, all the molecules were aligned well in the active site, especially the scaffold.

Table 2 Statistical parameter of the CoMFA and CoMSIA models

Statistical parameters	CoMFA	CoMSIA
q^{2a}	0.691	0.660
ONC ^b	3	4
SEE ^c	0.355	0.241
r^{2d}	0.914	0.961
F value ^e	140.821	241.387
r_{pred}^{2f}	0.902	0.937
<i>Fraction of field contributions</i>		
Steric	0.584	0.111
Electrostatic	0.416	0.271
Hydrophobic	–	0.307
Hydrogen bond donor	–	0.146
Hydrogen bond acceptor	–	0.165

^a Leave one out (LOO) cross-validated correlation coefficient

^b Optimum number of components

^c Standard error of estimate

^d Non-cross-validated correlation efficient

^e F test value

^f Predicted correlation coefficient for the test set

3D-QSAR statistics

The CoMFA model developed based on two fields (S and E) gave a cross-validated coefficient r_{cv}^2 of 0.691 with an optimal components of 3, r_{ncv}^2 of 0.914, SEE of 0.355 and F value of 140.821. The corresponding field contributions of parameters were 58.4 and 41.6 %. The CoMSIA model developed based on five fields (S, E, H, D and A), giving the cross-validated coefficient r_{cv}^2 of 0.660 with an optimal components of 4, r_{ncv}^2 of 0.961, SEE of 0.241 and F value of 241.387, was employed for detailed analysis. The corresponding field contributions of parameters were 11.1, 27.1, 30.7, 14.6 and 16.5 %. The statistical parameters above indicated that these two models were statistically significant (Table 2). Figure 3 depicted the relationship between the predicted and experimental pIC_{50} values for the non-cross validated coefficient of the two models. The predicted values

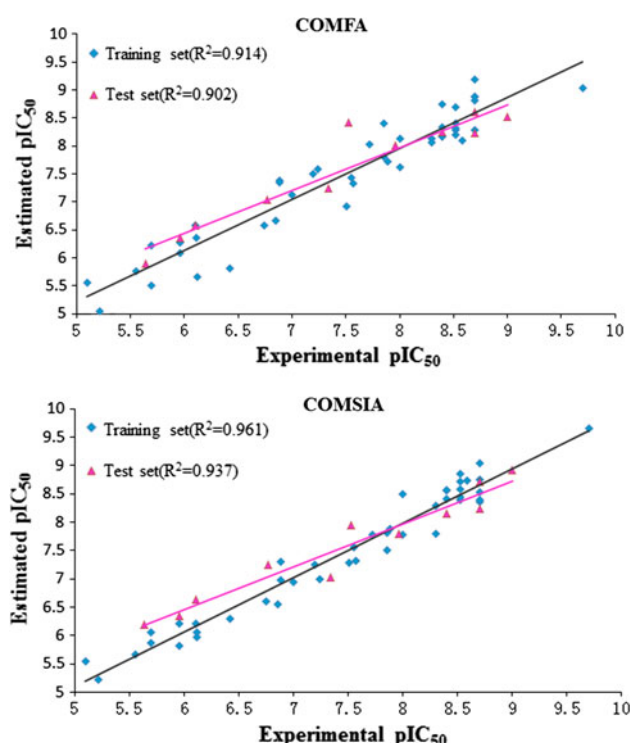


Fig. 3 Correlation between the predicted and experimental activities of the training and test set compounds (CoMFA and CoMSIA models)

did not deviate significantly from the actual values (generally less than one logarithmic unit, Table 3). The R^2_{pre} value was 0.914 and 0.961, indicating very high internal predictability.

Validation of the 3D-QSAR models

An external test set of 11 compounds was used to further validate the external predictive ability (Table 1). Satisfactory results were obtained by predictive correlation coefficient R^2_{pre} of 0.902 and 0.937 (Fig. 3). The favourable R^2_{pre} values indicated reliable external predictive ability. These statistical data and graph indicated that the predicted pIC_{50} values agreed well with the experimental values in a tolerable error range. Besides, considering that the steric and electrostatic fields in CoMFA analysis were also included in CoMSIA analysis and better predictive ability reflected by R^2_{pre} , CoMSIA model should be applied in the evaluation of new molecules generated by this fragment-based strategy.

Contour maps

Since the steric and electrostatic contour map obtained in CoMFA analysis were similar with that in CoMSIA analysis, only the CoMSIA model was visualized as 3D contour maps aligned into the active site. As the CoMSIA model was derived from docking conformations, it

considered both ligands and the active site properties. Therefore, the contour maps would be discussed in combination of both ligand and receptor. Compound 51 was used as the reference ligand for understanding the results.

For the steric contour map (Fig. 4), it was observed that there were three maps located in the binding site. The green contour map suggested it was sterically favored. Considering the spatial position of this substituted group in the binding site, it has extended into the solvent accessible region. Big hydrophilic fragments were suitable for this substituted point. Besides, from known inhibitors, compounds with such substituted groups have better bioactivity like compound 51. The group linking the hydrophilic fragments to the scaffold should not be too big as a yellow contour map appeared around the pyrazole of compound 51. From Fig. 4, it located in the narrow region edged by the amino acid residues Tyr1159, Ile1084 and His1094. Therefore, the linker fragment should also keep the planarity of the pyrimidine ring of the scaffold. The other yellow contour map appeared around the substituted groups for R2. It covered the spatial region of the fragments linking the hydrophilic groups and the scaffold. Arg1084 and Arg1208 constituted the ‘canopy’ and ‘floor’ of the linker groups respectively. The size of the linker groups was limited by this narrow region to avoid possible spatial clashes.

The electrostatic protein surface was shown in combination with the CoMSIA electrostatic contour maps (Fig. 5). It should be noted that from red to blue of the surface, the electrostatic was changed from most positive to negative while it was opposite for the CoMSIA contour map. One blue contour map was found above the ligand entrance region, thus, groups with positive potential would be beneficial for activity. The colour of the electrostatic surface was about neutral to negative in this region, consistent with the blue contour map. Another blue contour map was found to cover the middle ring of the scaffold, in the proximity of the carbon atom of the carbonyl group, indicating that this position should be of positive potential. From the structures of ligands, the carbonyl group should be the most suitable one since it was electro-withdrawing. The other blue contour map was found in the proximity of the sulfamine. Compared with other substituted groups, compounds with sulfamine on this position got better activity. Although the contour map is not consistent with the electrostatic surface, structural optimization should be considered here for better activity. The red contour map was found to cover the methyl. Considering the positive potential of Arg1208 in the proximity of this methyl, it was not suitable for positive groups in this position.

Hydrophobic contour map was shown under the background of receptor lipophilic potential (Fig. 6). The

Table 3 Experimental and predicted activities for training and test set compounds of the CoMFA and CoMSIA models

Compd.	Actual	CoMFA		CoMSIA	
		Predicted	Residues	Predicted	Residues
1	7.51	6.913	0.597	7.282	0.228
2	5.96	6.084	−0.124	5.816	0.144
3	6.11	6.582	−0.472	6.208	−0.098
4	6.42	5.805	0.615	6.301	0.119
5	5.96	6.279	−0.319	6.211	−0.251
6	5.21	5.047	0.163	5.213	−0.003
7 ^a	7.03	7.425	−0.395	7.416	−0.386
8	7.33	7.844	−0.514	7.688	−0.358
9	6.36	6.826	−0.466	6.805	−0.445
10	7.05	6.580	0.47	6.901	0.149
11	7.49	7.297	0.193	7.181	0.309
12 ^a	7.62	7.142	0.478	8.146	−0.526
13	7.80	7.613	0.187	7.962	−0.162
14 ^a	6.55	7.245	−0.695	7.029	−0.479
15	6.74	6.578	0.162	6.602	0.138
16	7.19	7.505	−0.315	7.255	−0.065
17	8.00	7.622	0.378	7.774	0.226
18	7.85	7.805	0.045	7.804	0.046
19 ^a	6.77	7.038	−0.268	7.242	−0.472
20	8.40	8.747	−0.347	8.553	−0.153
21	7.72	8.019	−0.299	7.774	−0.054
22	8.30	8.137	0.163	8.280	0.020
23 ^a	7.96	8.015	−0.055	7.793	0.167
24	7.57	7.331	0.239	7.312	0.258
25	6.89	7.374	−0.484	6.973	−0.083
26	7.00	7.128	−0.128	6.935	0.065
27	7.89	7.714	0.176	7.876	0.014
28 ^a	8.40	8.241	0.159	8.145	0.255
29	8.70	8.275	0.425	8.361	0.339
30	8.70	8.881	−0.181	8.527	0.173
31	8.40	8.334	0.066	8.561	−0.161
32	8.52	8.205	0.315	8.578	−0.058
33	8.52	8.287	0.233	8.393	0.127
34 ^a	9.00	8.528	0.472	8.927	0.073
35	8.52	8.692	−0.172	8.71	−0.19
36	8.70	8.81	−0.11	8.754	−0.054
37	9.70	9.025	0.675	9.655	0.045
38	6.89	7.341	−0.451	7.297	−0.407
39	8.52	8.394	0.126	8.847	−0.327
40 ^a	8.70	8.608	0.092	8.721	−0.021
41	8.40	8.165	0.235	8.401	−0.001
42	8.70	9.18	−0.48	9.039	−0.339
43 ^a	7.52	8.426	−0.906	7.951	−0.431
44	7.24	7.592	−0.352	6.997	0.243
45	8.00	8.129	−0.129	8.49	−0.49
46	8.30	8.063	0.237	7.792	0.508
47	8.52	8.321	0.199	8.446	0.074

Table 3 continued

Compd.	Actual	CoMFA		CoMSIA	
		Predicted	Residues	Predicted	Residues
48 ^a	8.70	8.239	0.461	8.24	0.46
49	7.85	8.402	−0.552	7.496	0.354
50	8.70	8.877	−0.177	8.387	0.313
51	8.59	8.097	0.493	8.738	−0.148
52	7.55	7.426	0.124	7.552	−0.002
53 ^a	5.64	5.898	−0.258	6.193	−0.553
54	5.55	5.752	−0.202	5.657	−0.107
55	6.11	6.359	−0.249	6.057	0.053

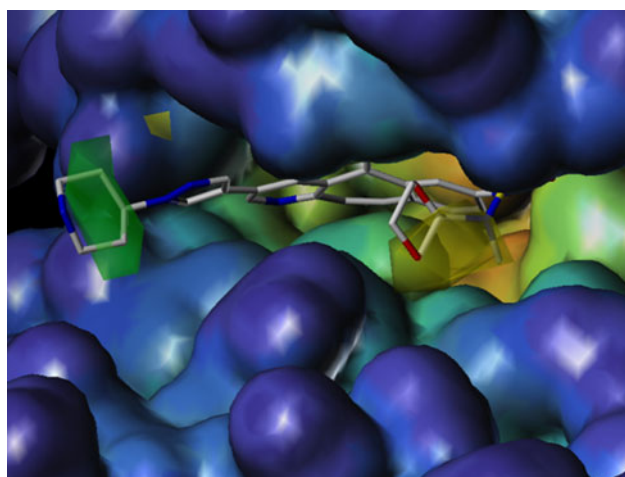
^a Test set compounds

Fig. 4 The steric contour maps were shown in combination of compound 51 under the background of cavity depth surface. *Green contour maps* indicate regions where bulky groups were beneficial for improving activity, whereas *yellow ones* meant bulky groups are not favored for better activity. The color from *blue* to *red* of cavity depth surface meant low to high depth inside the receptor

CoMSIA analysis gave two contour maps in total, both of which covered the R1 group. The yellow one was inside the ATP binding pocket, in proximity of the hinge residues like Met1160. Hydrophobicity was required for groups located in this region which was also indicated by the brown colour of the lipophilic surface. The other contour map was outside the ATP binding site, extending into the solvent accessible region. These two indications were in consistency with each other that hydrophilic groups were beneficial for better activity. Actually, group R2 also extended into the solvent accessible region, and there was no contour map shown according to the ligands. From their structures, it could be found that groups substituted in this position were almost hydrophilic. There were no significant changes of activity derived from hydrophobicity of these groups. Comparatively, there were significant changes of hydrophobicity of R1 groups. Therefore, CoMSIA analysis only gave suggestions on R1 groups.

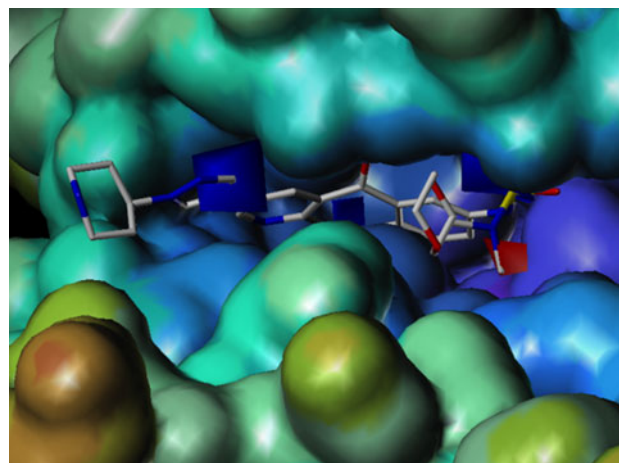


Fig. 5 The electrostatic contour maps were shown in combination with compound 51 under the background of electrostatic potential surface colored from *purple* (most negative) to *red* (most positive). *Blue contour maps* indicated regions where positive groups were beneficial for improving activity, whereas *red ones* meant negative groups were favored

Hydrogen bonds are very important for the binding and activity of kinase inhibitors. The CoMSIA model also gave hydrogen bond donor and acceptor fields for facilitating structural optimization. The hydrogen bonding contour maps were shown under the background of hydrogen bonding potential surface (Fig. 7). There were three colors of the hydrogen bonding potential surface, red, blue and gray representing hydrogen bond donor, receptor and no hydrogen bonds, respectively. For hydrogen bond donor contour map, a cyan one was found between the nitrogen atom of sulfamine and the oxygen atom of Asp1222, indicating fragments with hydrogen bond donor were preferable in this region. The blue hydrogen bonding potential surface was consistent with the cyan contour map. A purple contour map was found in the proximity of Arg1086, indicating fragments with hydrogen bond donor features were not suitable for this region. The hydrogen bond accepted from Arg1086 was beneficial for the

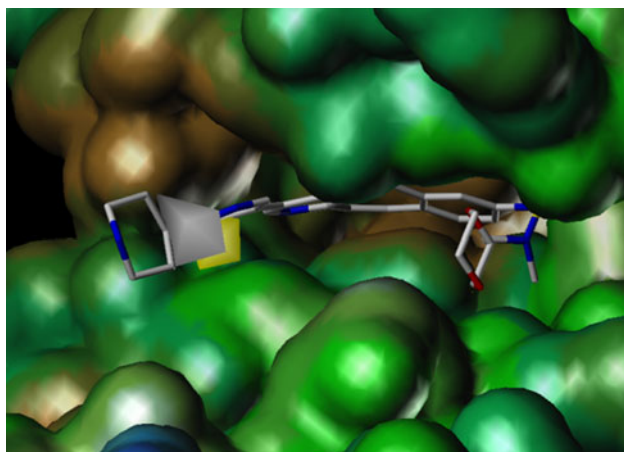


Fig. 6 The hydrophobic contour maps were shown in combination with compound 51 under the background of lipophilic potential surface colored from brown (highest hydrophobic) to blue (highest hydrophilic). Yellow contour maps (hydrophobic groups were favored); white (hydrophobic groups were disfavored)

ligand's activity. Therefore, hydrogen bond acceptor was suitable in this region, which was also indicated by the magenta hydrogen bond acceptor contour map. The other red contour map was found in the proximity of pyrazole ring, between Ile1084 and Gly1163, indicating that hydrogen acceptor was not suitable in this area. From the color of hydrogen bond potential, gray surface beneath and blue surface above also indicated hydrogen bond acceptor was not suitable in this region. The contour maps and hydrogen bond potential surface agreed well with each other.

SAR summary for R groups

The *Ligand Interactions* module implemented in MOE 2009 was used to show the protein–ligand interaction of the compound (Fig. 8). In the ligand interaction figure, the

hydrogen bonds formed between the ligand and Asp1086 and Asp1222 were in consistent with the CoMSIA hydrogen bond contour maps. Besides, the hydrogen bond between the ligand and the hinge residue Met1160 was also important for receptor–ligand binding. The narrow shape indicated that linkers between the scaffold and fragments in the solvent accessible region should not be bulky. But the hydrophilic fragments of R1 located in the solvent accessible region outside ligand entrance should be bulky. On the contrary, the hydrophilic fragments of R2 located in the solvent accessible region should not be bulky as they just occupied the spatial position limited by the ‘canopy’ and ‘floor’. Besides, since linker1 located inside the ligand entrance region, it should be more hydrophobic compared with the fragments located in the solvent accessible region.

Structural insights obtained from 3D-QSAR models in combination with protein–ligand interaction analysis would provide requirements of pharmacophoric features for R groups. Keeping the scaffold still, the double bond of the central seven-membered ring should not be saturated and the carbonyl should not be replaced by other groups like hydroxyl. For R1, hydrophilic fragments of large size should be beneficial for improving activity. Linker1 should be hydrophobic fragments of medium or small size. For R2, hydrophilic fragments of medium size with hydrogen bond acceptor should be suitable. Linker2 was also very important since it would provide a hydrogen bond to Asp1222 and accept a possible hydrogen bond from Arg1086. Besides, linker2 should be flexible fragments of small size with hydrogen bond donor and acceptor. The detailed information about pharmacophoric features for R groups were shown in Fig. 9.

Sitemap was also used for active site analysis. Different from *Ligand Interaction* module in MOE, it gives information on characteristics of binding sites, including site points, hydrophobic and hydrophilic maps. In the generated site maps, it was found that the active region located by

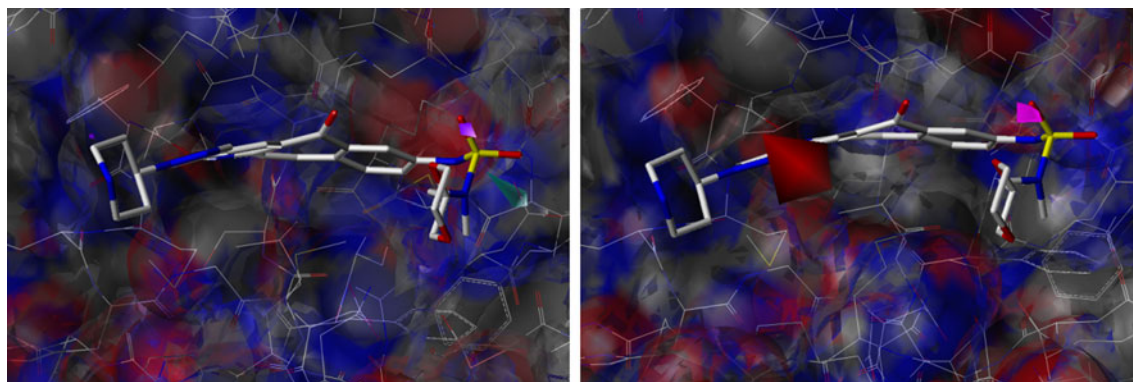


Fig. 7 The contour maps of HBD and HBA were shown in combination with compound 5. Cyan (HBD favored); purple (HBD disfavored); magenta (HBA favored); red (HBA disfavored)

Fig. 8 The protein–ligand interactions (PDB ID: 3R7O) provided by *Ligand Interactions* module implemented in MOE2009

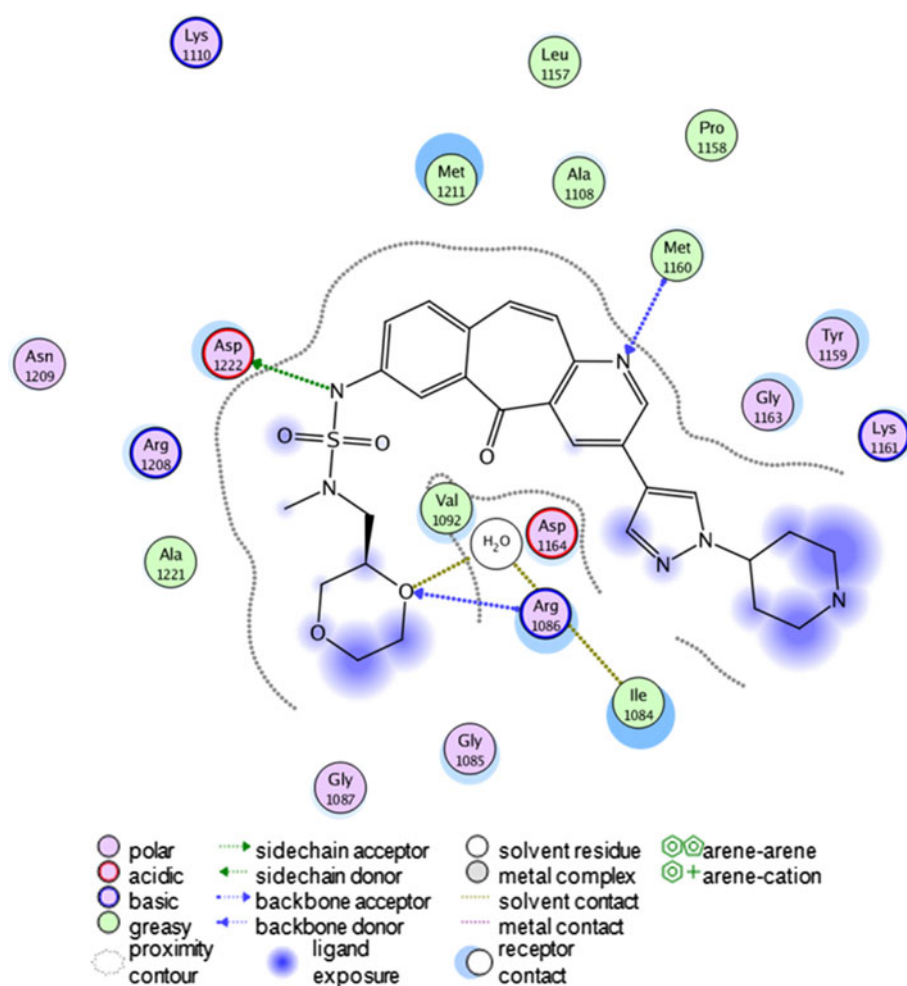


Fig. 9 SAR summarization for R groups

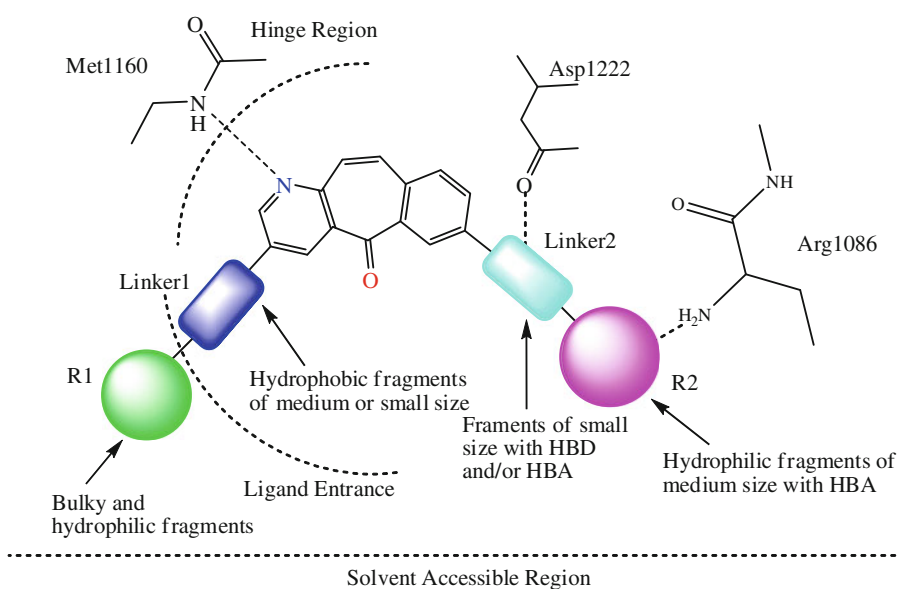
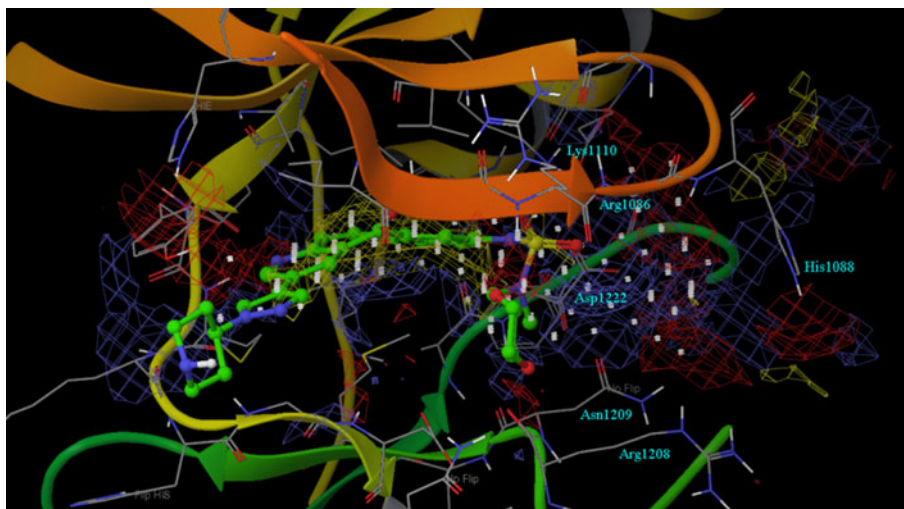


Fig. 10 Site maps generated using *Sitemap*: the ligand was compound 51, *white points* represented the location of identified active region, *yellow mesh map* represented hydrophobic regions, *blue* and *red mesh maps* represented hydrogen bond donors and acceptors, respectively



white points was not consistent with the active site represented by the co-crystal ligand (Fig. 10). The new identified active region extended in the direction of His1088. Besides, R1 and R2 were not completely covered by the white points. The yellow mesh map represented hydrophobic region in the active region. It covered the scaffold and linker1, consistent with the results of 3D-QSAR. Besides the hinge region, the spatial space occupied by linker2 and R2, and the new identified region were considered as hydrogen bond rich regions. The first two regions were consistent with those observed in 3D-QSAR. The new identified region was rimmed by Asp1222, Arg1208, Asn1209, and Arg1086 to His1088, and hydrogen bonds could be found between the ligand and Arg1086, Asp1222 and Arg1208. Compared with the known active site, the direction for linker2 and R2 should be changed to the new hydrogen bond rich region, which was also hydrophilic. But the pharmacophoric features for linker2 and R2 were not changed. Therefore, information given by the active site analysis was that linker2 and R2 should change their direction to explore the new active region. This new active site would be used to filter the new molecular library. The final result would prove whether this new proposal for the active site was really beneficial for improving activity.

Fragment identification and combination

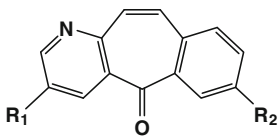
The structural insights obtained from 3D-QSAR and active site analysis confirmed the pharmacophoric features for R groups, which were converted into queries in MOE 2009. They were applied to screen the Zinc fragment library. There were 1,416 fragments satisfied the requirements for R1 while 2,149 fragments suitable for R2. The module of *scaffold replacement* was used to add R1 and R2 groups to

the scaffold, and *Breed* was subsequently used to generate new molecules with the method of cross combination. Finally, 12,012 new molecules were obtained after filtered by “Rule of 5” and duplicate filtration.

Evaluation of new molecules

Virtual screening was performed against the new molecule library, and the binding mode of the new molecules was considered as the first important criteria in the process of virtual screening. It was found that 6,363 molecules could keep the interactions between the scaffold and protein, and their docking conformations aligned well in the active site, especially the scaffold, providing the premise for 3D-QSAR prediction. The CoMSIA model was applied to predict their activity. Compounds with a pIC_{50} value greater than 9.0 were kept for protein–ligand interaction fingerprint analysis. In combination with visual inspection, 27 molecules were considered as the potential molecules (Table 4).

The new identified active region was also used to map these potential molecules. One of the potential molecules, S15, mapped well on the newly identified active region, extended in the direction of the new hydrogen bond rich region (Fig. 11). It got a predicted activity of pIC_{50} 9.192, indicating it a potential active c-Met inhibitor. Bioactivity should be given to prove the effectiveness of our fragment-based strategy and the druggability of the new active site. When we were making biological evaluation on this molecule, it was reported to be a highly active c-Met inhibitor (IC_{50} 1 nM) [38], which proved robust predictability of the CoMSIA model. This also strongly demonstrated the effectiveness of the fragment-based strategy and the druggability of the new explored hydrogen bond rich region. Given the success of S15, other potential

Table 4 Potential molecules provided by the fragment-based strategy for structural optimization


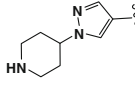
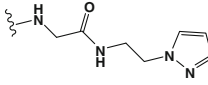
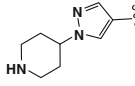
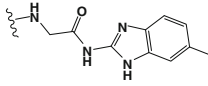
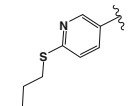
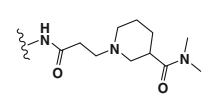
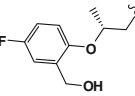
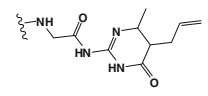
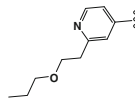
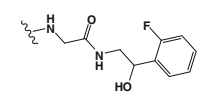
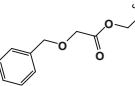
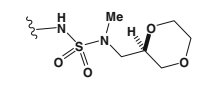
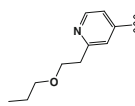
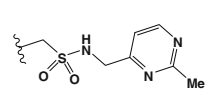
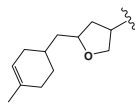
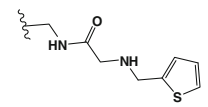
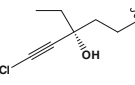
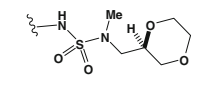
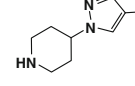
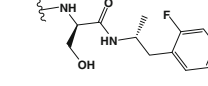
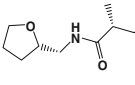
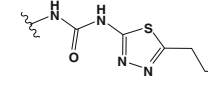
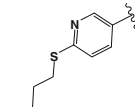
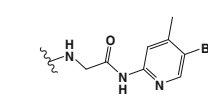
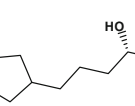
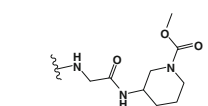
Compd.	R ₁	R ₂	Predicted pIC ₅₀	GScore	IC ₅₀
S1			9.659	−11.22	
S2			9.583	−11.04	
S3			9.549	−11.11	
S4			9.508	−11.94	
S5			9.388	−10.93	
S6			9.364	−10.59	
S7			9.345	−11.13	
S8			9.309	−10.36	
S9			9.278	−10.20	
S10			9.254	−11.18	
S11			9.248	−11.45	
S12			9.235	−11.12	
S13			9.201	−10.73	

Table 4 continued

S14			9.197	−11.08
S15 (MK-8033)			9.192	−11.11 1 nM
S16			9.187	−10.33
S17			9.169	−10.83
S18			9.148	−11.13
S19			9.122	−10.53
S20			9.073	−10.77
S21			9.052	−11.11
S22			9.042	−11.15
S23			9.038	−11.47
S24			9.033	−11.20
S25			9.028	−10.02
S26			9.009	−10.69
S27			9.001	−10.37

Fig. 11 Site maps generated using *Sitemap*: the ligand was compound S15, *white points* represented the new identified active region, *yellow mesh map* represented hydrophobic regions, *blue* and *red mesh maps* represented hydrogen bond donors and acceptors, respectively

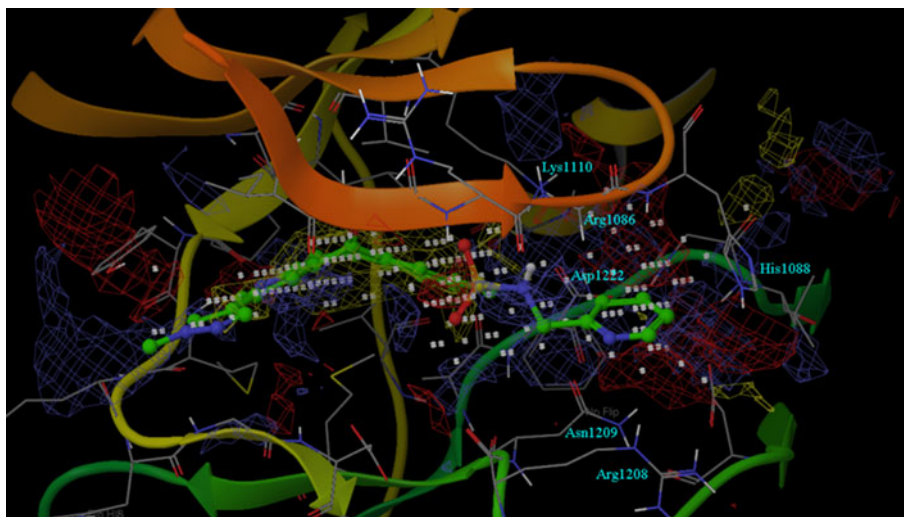
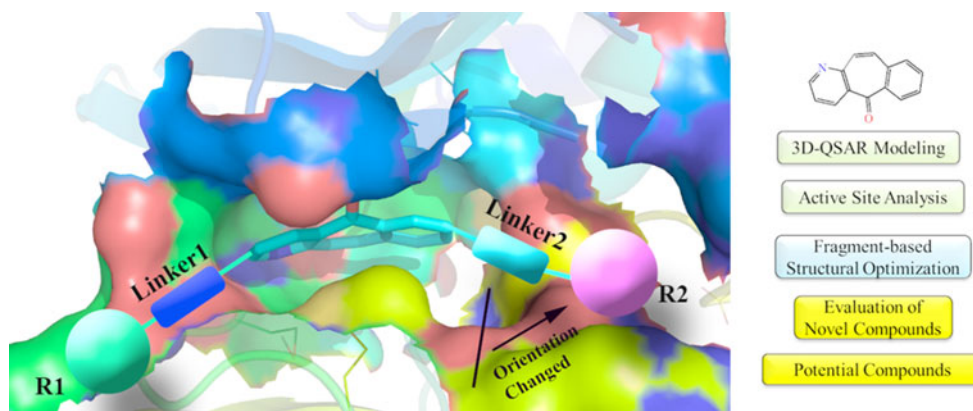


Fig. 12 3D-QSAR and active site analysis provided specific pharmacophoric requirements of R groups used in this fragment-based strategy for molecular optimization



compounds in the list were predicted to be active c-Met inhibitors.

Conclusions

A novel fragment-based strategy in combination with 3D-QSAR was proposed in this study. It was evaluated by applying it in structural optimization on the scaffold of 5H-benzo[4,5]cyclohepta[1,2-b]pyridin-5-one for developing c-Met inhibitors. 3D-QSAR models including CoMFA and CoMSIA were constructed, which were rigorously validated using external test set, showing reliability to predict activity for compounds of this series. Protein–ligand interaction analysis by MOE2009 and the contour maps generated by 3D-QSAR models were analyzed to give a SAR summary for R groups. The site maps generated by *Sitemap* explored a new active region not consistent with the previous active site. Although the direction for R2 to extend was changed, the requirements of pharmacophoric features for R2 were almost the same. Therefore, the SAR

results for R1 and R2 were applied for fragment screening, respectively. The obtained suitable fragments were added to the scaffold separately and then hybridized using *BREED*. Molecular docking, activity prediction by the CoMSIA model, and visual inspection applied to the new molecular library resulted in 27 potential molecules. The compound S15, well mapped onto the new explored active site, was newly reported to be an active c-Met inhibitor.

Compared with other studies, the fragment-based strategy in this study focused on structural optimization. The strategy consisted of several parts, including 3D-QSAR modeling, active site analysis, fragment-based structural optimization and evaluation of new molecules. The evaluation study resulted in an active c-Met inhibitor with good inhibitory activity, proving the effectiveness of the fragment-based strategy and the druggability of the newly explored active site. The key procedure of this strategy was the confirmation of the SAR for R groups. 3D-QSAR and active site analysis could provide sufficient information for this procedure, which could also be used to screen the new molecular library. Therefore, it was feasible to combine

them with the fragment-based methods for structural optimization (Fig. 12). The evaluation results of this fragment-based strategy indicated its potential application to facilitate lead optimization against other targets.

Acknowledgments The authors thank Dr. Huifang Li (the University of British Columbia) for her help in drafting the manuscript. This work was supported by National Natural Science Foundation of China (81172933, 21102181 and 30973609); Fundamental Research Funds for the Central Universities (2J10004, JKZ2011004 and JKY2011020); Jiangsu Provincial Graduate Innovation Research Foundation (CXZZ12_0315); State Key Laboratory of Natural Medicines (China Pharmaceutical University) Foundation for major research projects (SKLNMZZ201205); and Specialized Research Fund for the Doctoral Program of Higher Education (No. 20100096110007).

References

- Desjarlais RL (2011) Using computational techniques in fragment-based drug discovery. *Methods Enzymol* 493:137–155
- Kumar A, Voet A, Zhang KY (2012) Fragment based drug design: from experimental to computational approaches. *Curr Med Chem* 19:5128–5147
- Baker M (2013) Fragment-based lead discovery grows up. *Nat Rev Drug Discov* 12:5–7
- Villar HO, Hansen MR (2007) Computational techniques in fragment based drug discovery. *Curr Top Med Chem* 7: 1509–1513
- Law R, Barker O, Barker JJ, Hestekamp T, Godemann R, Andersen O, Fryatt T, Courtney S, Hallett D, Whittaker M (2009) The multiple roles of computational chemistry in fragment-based drug design. *J Comput Aided Mol Des* 23:459–473
- Sheng C, Zhang W (2013) Fragment informatics and computational fragment-based drug design: an overview and update. *Med Res Rev* 33:554–598
- Yuan H, Lu T, Ran T, Liu H, Lu S, Tai W, Leng Y, Zhang W, Wang J, Chen Y (2011) Novel strategy for three-dimensional fragment-based lead discovery. *J Chem Inf Model* 51:959–974
- Erlanson DA, McDowell RS, O'Brien T (2004) Fragment-based drug discovery. *J Med Chem* 47:3463–3482
- Cramer RD, Patterson DE, Bunce JD (1988) Comparative molecular field analysis (CoMFA). 1. Effect of shape on binding of steroids to carrier proteins. *J Am Chem Soc* 110:5959–5967
- Klebe G, Abraham U, Mietzner T (1994) Molecular similarity indices in a comparative analysis (CoMSIA) of drug molecules to correlate and predict their biological activity. *J Med Chem* 37: 4130–4146
- Katz JD, Jewell JP, Guerin DJ, Lim J, Dinsmore CJ, Deshmukh SV, Pan BS, Marshall CG, Lu W, Altman MD, Dahlberg WK, Davis L, Falcone D, Gabarda AE, Hang G, Hatch H, Holmes R, Kunii K, Lumb KJ, Lutterbach B, Mathvink R, Nazef N, Patel SB, Qu X, Reilly JF, Rickert KW, Rosenstein C, Soisson SM, Spencer KB, Szwczak AA, Walker D, Wang W, Young J, Zeng Q (2011) Discovery of a 5H-benzo[4,5]cyclohepta[1,2-b]pyridin-5-one (MK-2461) inhibitor of c-Met kinase for the treatment of cancer. *J Med Chem* 54:4092–4108
- Underiner TL, Herbertz T, Miknyoczki SJ (2010) Discovery of small molecule c-Met inhibitors: evolution and profiles of clinical candidates. *Anticancer Agents Med Chem* 10:7–27
- Zou HY, Li Q, Lee JH, Arango ME, McDonnell SR, Yamazaki S, Koudriakova TB, Alton G, Cui JJ, Kung PP, Nambu MD, Los G, Bender SL, Mroczkowski B, Christensen JG (2007) An orally available small-molecule inhibitor of c-Met, PF-2341066, exhibits cytoreductive antitumor efficacy through antiproliferative and antiangiogenic mechanisms. *Cancer Res* 67:4408–4417
- Bellon SF, Kaplan-Lefko P, Yang Y, Zhang Y, Moriguchi J, Rex K, Johnson CW, Rose PE, Long AM, O'Connor AB, Gu Y, Coxon A, Kim TS, Tasker A, Burgess TL, Dussault I (2008) c-Met inhibitors with novel binding mode show activity against several hereditary papillary renal cell carcinoma-related mutations. *J Biol Chem* 283:2675–2683
- Pan BS, Chan GK, Chenard M, Chi A, Davis LJ, Deshmukh SV, Gibbs JB, Gil S, Hang G, Hatch H, Jewell JP, Kariv I, Katz JD, Kunii K, Lu W, Lutterbach BA, Paweletz CP, Qu X, Reilly JF, Szwczak AA, Zeng Q, Kohl NE, Dinsmore CJ (2010) MK-2461, a novel multitargeted kinase inhibitor, preferentially inhibits the activated c-Met receptor. *Cancer Res* 70:1524–1533
- Berthou S, Aebersold DM, Schmidt LS, Stroka D, Heigl C, Streit B, Stalder D, Gruber G, Liang C, Howlett AR, Candinas D, Greiner RH, Lipson KE, Zimmer Y (2004) The Met kinase inhibitor SU11274 exhibits a selective inhibition pattern toward different receptor mutated variants. *Oncogene* 23:5387–5393
- Qi J, McTigue MA, Rogers A, Lifshits E, Christensen JG, Janne PA, Engelman JA (2011) Multiple mutations and bypass mechanisms can contribute to development of acquired resistance to MET inhibitors. *Cancer Res* 71:1081–1091
- Dussault I, Bellon SF (2008) c-Met inhibitors with different binding modes: two is better than one. *Cell Cycle* 7:1157–1160
- Lipinski CA (2004) Lead- and drug-like compounds: the rule-of-five revolution. *Drug Discov Today Technol* 1:337–341
- Rickert KW, Patel SB, Allison TJ, Byrne NJ, Darke PL, Ford RE, Guerin DJ, Hall DL, Kornienko M, Lu J, Munshi SK, Reid JC, Shipman JM, Stanton EF, Wilson KJ, Young JR, Soisson SM, Lumb KJ (2011) Structural basis for selective small molecule kinase inhibition of activated c-Met. *J Biol Chem* 286:11218–11225
- Kontoyianni M, McClellan LM, Sokol GS (2004) Evaluation of docking performance: comparative data on docking algorithms. *J Med Chem* 47:558–565
- Sandor M, Kiss R, Keseru GM (2010) Virtual fragment docking by Glide: a validation study on 190 protein-fragment complexes. *J Chem Inf Model* 50:1165–1172
- Halgren T (2007) New method for fast and accurate binding-site identification and analysis. *Chem Biol Drug Des* 69:146–148
- Pierce AC, Rao G, Bemis GW (2004) BREED: generating novel inhibitors through hybridization of known ligands. Application to CDK2, p38, and HIV protease. *J Med Chem* 47:2768–2775
- Rees DC, Congreve M, Murray CW, Carr R (2004) Fragment-based lead discovery. *Nat Rev Drug Discov* 3:660–672
- Larsson EA, Jansson A, Ng FM, Then SW, Panicker R, Liu B, Sangthongpitag K, Pendharkar V, Tai SJ, Hill J, Dan C, Ho SY, Cheong WW, Poulsen A, Blanchard S, Lin GR, Alam J, Keller TH, Nordlund P (2013) Fragment-based ligand design of novel potent inhibitors of tankyrases. *J Med Chem* 56:4497–4508
- Wyatt PG, Woodhead AJ, Berdini V, Boulstridge JA, Carr MG, Cross DM, Davis DJ, Devine LA, Early TR, Feltell RE, Lewis EJ, McMenamin RL, Navarro EF, O'Brien MA, O'Reilly M, Reule M, Saxty G, Seavers LC, Smith DM, Squires MS, Trewartha G, Walker MT, Woolford AJ (2008) Identification of N-(4-piperidinyl)-4-(2,6-dichlorobenzoylamino)-1H-pyrazole-3-carboxamide (AT7519), a novel cyclin dependent kinase inhibitor using fragment-based X-ray crystallography and structure based drug design. *J Med Chem* 51:4986–4999
- Dey F, Caflisch A (2008) Fragment-based de novo ligand design by multiobjective evolutionary optimization. *J Chem Inf Model* 48:679–690
- Urich R, Wishart G, Kiczun M, Richters A, Tidten-Luksch N, Rauh D, Sherborne B, Wyatt PG, Brenk R (2013) De novo design

- of protein kinase inhibitors by in silico identification of hinge region-binding fragments. *ACS Chem Biol* 8:1044–1052
30. Chen H, Yang Z, Ding C, Chu L, Zhang Y, Terry K, Liu H, Shen Q, Zhou J (2013) Fragment-based drug design and identification of HJC0123, a novel orally bioavailable STAT3 inhibitor for cancer therapy. *Eur J Med Chem* 62:498–507
 31. Congreve M, Chessari G, Tisi D, Woodhead AJ (2008) Recent developments in fragment-based drug discovery. *J Med Chem* 51:3661–3680
 32. Fischer M, Hubbard RE (2009) Fragment-based ligand discovery. *Mol Interv* 9:22–30
 33. Fattori D, Squarcia A, Bartoli S (2008) Fragment-based approach to drug lead discovery: overview and advances in various techniques. *Drugs R D* 9:217–227
 34. Rognan D (2012) Fragment-based approaches and computer-aided drug discovery. *Top Curr Chem* 317:201–222
 35. Kolb P, Kipouros CB, Huang D, Caflisch A (2008) Structure-based tailoring of compound libraries for high-throughput screening: discovery of novel EphB4 kinase inhibitors. *Proteins* 73:11–18
 36. Zhu T, Lee H, Lei H, Jones C, Patel K, Johnson ME, Hevener KE (2013) Fragment-based drug discovery using a multidomain, parallel MD-MM/PBSA screening protocol. *J Chem Inf Model* 53(3):560–572
 37. Zhang Y, Liu H, Jiao Y, Yuan H, Wang F, Lu S, Yao S, Ke Z, Tai W, Jiang Y, Chen Y, Lu T (2012) De novo design of N-(pyridin-4-ylmethyl)aniline derivatives as KDR inhibitors: 3D-QSAR, molecular fragment replacement, protein–ligand interaction fingerprint, and ADMET prediction. *Mol Divers* 16:787–802
 38. Northrup AB, Katcher MH, Altman MD, Chenard M, Daniels MH, Deshmukh SV, Falcone D, Guerin DJ, Hatch H, Li C, Lu W, Lutterbach B, Allison TJ, Patel SB, Reilly JF, Reutershan M, Rickert KW, Rosenstein C, Soisson SM, Szewczak AA, Walker D, Wilson K, Young JR, Pan BS, Dinsmore CJ (2013) Discovery of 1-[3-(1-methyl-1H-pyrazol-4-yl)-5-oxo-5H-benzo[4,5]cyclohepta[1,2-b]pyridin-7-yl]-N-(pyridin-2-ylmethyl)methanesulfonamide (MK-8033): a specific c-Met/Ron dual kinase inhibitor with preferential affinity for the activated state of c-Met. *J Med Chem* 56:2294–2310